Flow-induced reconfiguration of buoyant and flexible aquatic vegetation

Flow induced reconfiguration of buoyant and flexible aquatic vegetation

Mitul Luhar* and Heidi M. Nepf

Department of Civil and Environmental Engineering, Massachusetts Institute of Technology, Cambridge, Massachusetts

*Corresponding author: mluhar@mit.edu

Acknowledgements

We thank two anonymous reviewers for insightful comments that greatly improved this manuscript. This material is based upon work supported by grant 0751358 from the National Science Foundation Ocean Sciences Division.

Abstract

Plant posture can play a key role in the health of aquatic vegetation, by setting drag, controlling light availability, and mediating the exchange of nutrients and oxygen. We study the flow-induced reconfiguration of buoyant, flexible aquatic vegetation through a combination of laboratory flume experiments and theoretical modeling. The laboratory experiments measure drag and posture for model blades that span the natural range for seagrass stiffness and buoyancy. The theoretical model calculates plant posture based on a force balance that includes posture-dependent drag and the restoring forces due to vegetation stiffness and buoyancy. When the hydrodynamic forcing is small compared to the restoring forces, the model blades remain upright and the quadratic law, $F_x \propto U^2$, predicts the drag well (F_x is drag, U is velocity). When the hydrodynamic forcing exceeds the restoring forces, the blades are pushed over by the flow, and the quadratic drag law no longer applies. The model successfully predicts when this transition occurs. The model also predicts that when the dominant restoring mechanism is blade stiffness, reconfiguration leads to the scaling $F_x \propto U^{4/3}$. When the dominant restoring mechanism is blade buoyancy, reconfiguration can lead to a sub-linear increase in drag with velocity, i.e., $F_x \propto U^a$ with $a < 1$. Laboratory measurements confirm both these predictions. The model also predicts drag and posture successfully for natural systems ranging from seagrasses to marine macroalgae of more complex morphology.

Introduction

The most obvious hydrodynamic effect of aquatic vegetation is that it provides resistance to flow. In the past, this has led to aquatic vegetation being removed from river channels to increase conveyance capacity and reduce flooding (Kouwen and Unny 1973). It is now recognized that aquatic vegetation provides many important ecosystem services by resisting flow and altering local flow conditions (Carpenter and Lodge 1986; Bouma et al. 2005; Peralta et al. 2008). By reducing the near-bed flow, benthic vegetation promotes the sedimentation of suspended material and inhibits sediment resuspension, thereby limiting erosion (Fonseca and Fisher 1986; Barko and James 1998). A reduction in suspended material leads to greater light penetration and enhanced productivity (Madsen et al. 2001; de Boer 2007). The ensuing low flow environment within vegetation beds serves as shelter for fish and aquatic invertebrates. However, these ecosystem services come at a cost – the vegetation must withstand the equal and opposite drag force exerted by the water, which can damage or dislodge the vegetation (Denny et al. 1998; Bouma et al. 2005).

Many aquatic macrophytes are flexible. They are pushed over into more streamlined postures with increasing velocity. Relative to rigid, upright vegetation, this reconfiguration leads to significantly reduced drag for flexible vegetation (Koehl 1984; Vogel 1994). In addition to setting drag, posture influences other processes important to the health of aquatic vegetation. For example, vegetation posture controls light availability. An upright posture exposes the vegetation to higher light intensities, while a streamlined posture increases the projected leaf area absorbing the incoming light but makes self-shading among neighboring macrophytes more likely (Zimmerman 2003). Posture can also control nutrient and oxygen exchange between the vegetation and the surrounding water. Faster flows perpendicular to the vegetation lead to thinner

54 diffusive boundary layers around the vegetation, which can enhance the rate of nutrient (Hurd
55 2000) and oxygen (Mass et al. 2010) transfer. In addition to regulating the health of the
56 vegetation, nutrient uptake and oxygen production provide an important ecosystem service:
57 aquatic vegetation prevents dangerous eutrophication and anoxia (Costanza et al. 1997). Previous
58 studies show that the morphology of aquatic vegetation can change in response to the local
59 hydrodynamic environment (Puijalon et al. 2005; Peralta et al. 2006; Stewart 2006), reflecting
60 the feedbacks between flow, plant posture and the biological processes described above.
61 Due to its importance to flood and ecosystem management, the physical interaction
62 between water flow and aquatic vegetation has received significant attention (Nikora 2010).
63 There have been numerous attempts to characterize the drag generated by flexible vegetation in
64 unidirectional currents starting with Kouwen and Unny (1973). However, a universal description
65 of reconfiguration and drag for flexible aquatic vegetation remains elusive (*see* discussion of
66 Sand-Jensen 2003 by Green 2005; Sukhodolov 2005; Statzner et al. 2006). Reconfiguration can
67 also be important for terrestrial vegetation in wind-exposed environments (Harder et al. 2004). In
68 a recent review concerning the effect of wind on plants, de Langre (2008) proposed a simple
69 reconfiguration model balancing the opposing moments due to aerodynamic drag and plant
70 stiffness that qualitatively reproduced the trends observed in experimental drag data. There is,
71 however, an important distinction between terrestrial and aquatic vegetation – aquatic vegetation
72 can be positively buoyant. Seagrass blades have gas-filled lacunae (Penhale and Wetzel 1983),
73 while kelps and other macroalgae have gas-filled floats called pneumatocysts (Denny et al. 1997;
74 Stewart 2006). As a result, hydrodynamic drag is resisted both by vegetation stiffness and
75 buoyancy (Stewart 2006).

Previous models examining the reconfiguration of aquatic vegetation, developed by Green (2005) and Abdelrhman (2007), consider vegetation stiffness to be negligible. Hence, these models are not universally applicable. A recent study by Dijkstra and Uittenbogaard (2010) does consider the interaction between flow and vegetation that is both buoyant and has non-negligible stiffness. However, Dijkstra and Uittenbogaard (2010) focus primarily on the effect of the vegetation on the flow structure, without addressing vegetation reconfiguration in detail. In this study, we focus on the effect of unidirectional flow on vegetation posture and drag, making our work complementary to that of Dijkstra and Uittenbogaard (2010). Alben et al. (2002, 2004) and Gosselin et al. (2010) show how the reconfiguration of flexible bodies depends on the relative magnitude of the drag force and the restoring force due to body stiffness. We extend these recent advances in our understanding of flow-induced reconfiguration for application to aquatic vegetation by explicitly considering both rigidity and buoyancy as restoring forces. For simplicity, we develop the model for individual blades with rectangular cross-sections characteristic of seagrasses. However, the same physical principles hold for other morphologically complex salt- and fresh-water vegetation. We show that the model is able to predict posture and drag for systems ranging from model blades (present study), to real seagrasses (Fonseca and Kenworthy 1987; Abdelrhman 2007), and marine macroalgae of complex morphology (Stewart 2006).

Methods

Theoretical model for buoyant, flexible vegetation in flow

To develop a model describing the flow-induced reconfiguration of buoyant, flexible seagrass blades, we start with a few simplifying assumptions. First, we assume that the blades can be modeled as isolated, buoyant, inextensible elastic beams of constant width (b), thickness

99 (t), density (ρ_v), and elastic modulus (E). Second, the horizontal velocity (U) is uniform over
100 depth. Third, we consider steady flow where the dominant hydrodynamic force is form drag.
101 Viscous skin friction is assumed to be negligible. Later, we discuss how the model can be
102 modified to account for more complex vegetation morphologies as well as spatial variations in
103 vegetation and flow properties. We also develop a formal criterion to indicate when skin friction
104 becomes important. Unsteady flows, such as those induced by surface waves, are not considered
105 in this paper.

106 We use the curvilinear coordinate system shown in Fig. 1, in which s is the distance along
107 the blade from the base and θ is the local bending angle of the blade relative to the vertical ($\theta = 0$
108 denotes an upright posture). The blade length is l, so that $s = l$ represents the tip of the blade.
109 Form drag, which derives from the velocity normal to the blade surface, is represented using a
110 standard quadratic law. The drag force per unit blade length is,

111 $$f_D = (1/2)\rho C_D b U^2 \cos^2\theta \qquad (1)$$

112 where ρ is the density of the water and C_D is the drag coefficient (Blevins 1984; Schouveiler et
113 al. 2005). The drag force is resisted by blade stiffness and blade buoyancy. The blade-normal
114 restoring force due to stiffness (V) is the spatial derivative of the internal bending moment, $M =$
115 $EI(d\theta/ds)$, i.e.,

116 $$V = -EI\frac{d^2\theta}{ds^2} \qquad (2)$$

117 where I ($=bt^3/12$) is the second-moment of area (Alben et al. 2002; Gosselin et al. 2010). The
118 vertical buoyancy force is

119 $$f_B = \Delta\rho g b t = (\rho - \rho_v) g b t \qquad (3)$$

per unit blade length. Here, $\Delta\rho$ is the density difference between the water and the blade, and g is gravitational acceleration.

The inset in Fig. 1 shows the blade-normal force balance for $s \geq s^*$, where s^* is an arbitrary position along the blade. This force balance yields the governing equation for posture:

$$V^*(s^*) + \int_{s^*}^{l} f_B \sin\theta^*(s^*)\,ds = \int_{s^*}^{l} \cos\big(\theta(s) - \theta^*(s^*)\big) f_D(\theta(s))\,ds \qquad (4)$$

(rigidity) (buoyancy) (drag)

V^* is the blade-normal restoring force due to stiffness at $s = s^*$, and θ^* is the bending angle at $s = s^*$. The buoyancy force acts vertically and so the component of the buoyancy force acting in the direction of V^* is $f_B \sin\theta^*$ per unit blade length. Hence, the integral on the left-hand side of Eq. 4 represents the projection in the direction of V^* of the total buoyancy force for $s \geq s^*$. Similarly, f_D is the blade-normal drag force per unit length, and so the integral on the right-hand side represents the projection in the direction of V^* of the total drag force for $s \geq s^*$. A force balance parallel to the blade would yield an expression for the blade tension at s^*. However, we do not explicitly calculate blade tension here.

Using the complete expressions for f_B (Eq. 3) and f_D (Eq. 1), and evaluating the integral on the left-hand side, Eq. 4 can be rewritten as:

$$-EI\left.\frac{d^2\theta}{ds^2}\right|_{s^*} + \Delta\rho g b t\big(l - s^*\big)\sin\theta^* = \frac{1}{2}\rho C_D b U^2 \int_{s^*}^{l} \cos\big(\theta - \theta^*\big)\cos^2\theta\, ds \qquad (5)$$

To make Eq. 5 dimensionless, we replace s with a normalized coordinate $\hat{s} = s/l$ so that $\hat{s} = 1$ represents the tip of the blade and $\hat{s}^* = s^*/l$ is an arbitrary position along the blade, as before. With this normalization, the curvature term in Eq. 5 scales as $|d^2\theta/ds^2| \sim 1/l^2$, and the restoring force due to blade stiffness scales as EI/l^2. This scaling is reasonable when the blade bends gradually over its entire length. For streamlined postures, however, the blades bend significantly

over a short distance close to the bed, producing curvature that is much larger than $1/l^2$. Therefore, we should keep in mind that the scale EI/l^2 underestimates the restoring force due to blade stiffness when bending occurs locally, e.g., only near the bed.

Dividing Eq. 5 by the factor EI/l^2 yields the following dimensionless equation for posture, i.e., describing $\theta^* = f(\hat{s}^*)$

$$-\left.\frac{d^2\theta}{d\hat{s}^2}\right|_{\hat{s}^*} + B(1-\hat{s}^*)\sin\theta^* = Ca\int_{\hat{s}^*}^{1}\cos(\theta-\theta^*)\cos^2\theta\, d\hat{s} \tag{6}$$

Posture is essentially controlled by two dimensionless parameters:

$$B = \frac{\Delta\rho g b t l^3}{EI} \tag{7}$$

$$Ca = \frac{1}{2}\frac{\rho C_D b U^2 l^3}{EI} \tag{8}$$

Physically, B represents the ratio of the restoring force due to buoyancy and the restoring force due to stiffness. We call this the buoyancy parameter. Ca is the Cauchy number, which indicates the relative magnitude of the hydrodynamic drag and the restoring force due to stiffness. Finally, we impose the following boundary conditions (Alben et al. 2002; Gosselin et al. 2010): the base of the blade is a clamped joint, $\theta = 0$ at $\hat{s} = 0$, and the tip of the blade is free, $d\theta/d\hat{s} = 0$ at $\hat{s} = 1$.

Crucially, B and Ca reflect the assumptions made in order to normalize Eq. 5. Specifically, the drag and buoyancy scales represent the maximum possible values for these forces, whereas the scale EI/l^2 can underestimate the stiffness restoring force, as discussed previously. The potential mismatch in scales is evident in Eq. 6. The term reflecting the buoyancy force is proportional to the factor $(1-\hat{s})\sin\theta$ which cannot exceed 1. Similarly, the value of the integral on the right-hand side, representing the drag force, also cannot exceed 1. However, the curvature term is unbounded. For streamlined postures, where blade curvature is

large close to the bed, $|d^2\theta/d\hat{s}^2| >> 1$, and the restoring force due to blade stiffness is larger than that suggested by the scale EI/l^2.

Reconfiguration reduces drag through two different mechanisms. First, reconfiguration reduces the frontal area of the vegetation, and second, the reconfigured shape tends to be more streamlined (de Langre 2008). To quantify the reduction of drag due to reconfiguration we propose an effective blade length, l_e. This is defined as the length of a rigid, vertical blade that generates the same horizontal drag as the flexible blade of total length l. In dimensionless terms, the effective length is:

$$\frac{l_e}{l} = \frac{\int_0^l (1/2)\rho C_D b U^2 \cos^3\theta \, ds}{(1/2)\rho C_D b l U^2} = \int_0^1 \cos^3\theta \, d\hat{s} \tag{9}$$

Based on this definition, the total horizontal drag force is $F_x = (1/2)\rho C_D b l_e U^2$, where the drag coefficient, C_D, for the flexible blades is identical to that for rigid, vertical blades. The effective length is equal to the blade length, $l_e = l$, if the blades remains upright in flow ($\theta = 0$). As the blades are pushed over ($\theta > 0$), the effective length decreases so that $l_e < l$. Note that the effective length defined in Eq. 9 accounts for drag reduction both due to the reduced frontal area in the reconfigured state, and due to the more streamlined shapes of the bent blades. In contrast, the deflected vegetation height, often used to quantify drag reduction due to reconfiguration, accounts only for a reduction in frontal area. For the coordinate system used here, the dimensionless deflected height of the blades is:

$$\frac{h}{l} = \int_0^1 \cos\theta \, d\hat{s} \tag{10}$$

Comparing Eqs. 9 and 10, it is clear that the effective length is always less than, or equal to, the deflected height, $l_e \leq h$.

Model predictions

Before describing the general case, where both blade buoyancy and stiffness play a role, we first consider the two limiting cases: zero stiffness and zero buoyancy. For the zero stiffness case, Eq. 6 simplifies to:

$$(1 - \hat{s}^*)\sin\theta^* = \left(B^{-1}Ca\right)\int_{\hat{s}^*}^{1} \cos(\theta - \theta^*)\cos^2\theta \, d\hat{s} \tag{11}$$

The parameter ($B^{-1}Ca$) represents the ratio of the drag force and the buoyancy force. With zero stiffness, the blade cannot sustain any internal bending moments. Hence, the boundary condition at the base of the vegetation changes from a clamped joint to a pin joint, $d\theta/d\hat{s} = 0$ at $\hat{s} = 0$. Further, because there is no restoring force due to blade curvature, the angle θ reflects the local balance between drag and buoyancy. Since the model does not consider any spatial variations in blade density or flow speed, the angle θ is constant along the blade. This is evident by balancing the blade-normal components of the forces shown in Eqs. 1 and 3. If b, t, $\Delta\rho$ and U are constant along $\hat{s}$, θ must also be. As a result, Eq. 11 simplifies further to:

$$\sin\theta = \left(B^{-1}Ca\right)\cos^2\theta \tag{12}$$

Eq. 12 can be solved easily to yield the blade angle, θ, as a function of ($B^{-1}Ca$). For θ constant along the blade, the blade remains straight as it tilts over (Fig. 2a, inset), and the effective blade length and deflected height are (l_e/l) = $\cos^3\theta$ and (h/l) = $\cos\theta$, respectively (Eqs. 9 and 10).

The predicted effective length for the zero-stiffness case is plotted as a function of the parameter ($B^{-1}Ca$) in Fig. 2a. The inset in Fig. 2a shows predicted postures for ($B^{-1}Ca$) = 0.1 and ($B^{-1}Ca$) = 3.2. When the hydrodynamic forcing is much smaller than the buoyancy force, ($B^{-1}Ca$) << 1, the blade remains upright in flow. Specifically, the effective length is approximately equal to the blade length, $0.9 < (l_e/l) < 1$ for ($B^{-1}Ca$) < 0.25. As the hydrodynamic forcing increases relative to the buoyancy force, the blade is pushed over and the effective length is reduced. As an

example, for $(B^{-1}Ca) = 3.2$, $\theta = 59°$, the effective length is $(l_e/l) = 0.14$, and the deflected height is $(h/l) = 0.52$, as shown in Fig. 2a. For $(B^{-1}Ca) >> 1$, the blade is pushed toward a near-horizontal posture, for which $\sin\theta \approx 1$, and Eq. 12 simplifies to $\cos\theta \sim (B^{-1}Ca)^{-1/2}$. In the limit of large $(B^{-1}Ca)$, therefore, the deflected height and effective length are $(h/l) \sim (B^{-1}Ca)^{-1/2}$ and $(l_e/l) \sim (B^{-1}Ca)^{-3/2}$, respectively (Fig. 2a). The Cauchy number (Eq. 8) is proportional to the square of the velocity, $Ca \propto U^2$, and so the above scaling implies that for $(B^{-1}Ca) >> 1$, the effective length is inversely proportional to the velocity cubed, $l_e \propto U^{-3}$, and the horizontal drag decreases with increasing velocity, $F_x \propto U^2 l_e \propto U^{-1}$. More generally, for $B^{-1}Ca > 1$, the effective length decreases with increasing velocity as $(l_e/l) \sim (B^{-1}Ca)^{-A}$, and so $l_e \propto U^{-2A}$, where the generic exponent, A, is greater than 0.5. Hence, the horizontal force, $F_x \propto U^2 l_e \propto U^{(2-2A)}$, increases sub-linearly with velocity, i.e., $F_x \propto U^a$ with $a = (2-2A) < 1$.

Next we consider the case where only blade stiffness is important – the zero-buoyancy case. For this case, the boundary condition at the base is a clamped joint, with $\theta = 0$ at $\hat{s} = 0$. Because $B = 0$, the governing Eq. 6 simplifies to:

$$-\left.\frac{d^2\theta}{d\hat{s}^2}\right|_{\hat{s}*} = Ca\int_{\hat{s}*}^{1} \cos(\theta - \theta*)\cos^2\theta \, d\hat{s} \qquad (13)$$

This equation for blade posture is solved to an accuracy of 10^{-3} in θ using an iterative shooting method (Stoer and Bulirsch 2002). The predicted effective length (Eq. 9) for the zero-buoyancy case is plotted against the Cauchy number in Fig. 2b, along with the predicted blade postures for $Ca = 1$ and $Ca = 32$. The model suggests that for $Ca < O(1)$, the hydrodynamic forcing is unable to overcome blade stiffness and the blade remains upright in flow. Specifically, the effective blade length is approximately equal to the blade length, $0.9 < (l_e/l) < 1$, for $Ca < 2$. For these conditions, the drag force increases with the square of velocity, $F_x \propto U^2$. However, as the Cauchy

number increases (U increasing), the blade is pushed over by the flow, and both the deflected height and effective blade length decrease. As an example, for $Ca = 32$ (inset, Fig. 2b), the effective length is $(l_e/l) = 0.30$ and the deflected height is $(h/l) = 0.61$ (Fig. 2b). Note that the decrease in effective length with increasing velocity (i.e., increasing Ca) is more gradual for the zero-buoyancy case compared to the zero-stiffness case described above (Fig. 2a).

The model predicts that for $Ca \gg 1$, the effective length scales as $(l_e/l) \sim Ca^{-1/3}$ (Fig. 2b). This scaling suggests that $l_e \propto Ca^{-1/3} \propto U^{-2/3}$ (c.f. $l_e \propto U^{-3}$ for the zero-stiffness case). Hence, the drag force increases with velocity as $F_x \propto U^2 l_e \propto U^{4/3}$, in agreement with the results obtained by Alben et al. (2002) and Gosselin et al. (2010) for non-buoyant bodies. The scaling $l_e/l \sim Ca^{-1/3}$ emerges directly from the balance of drag and the restoring force due to stiffness. For streamlined postures (e.g., Fig. 2b, inset, $Ca = 32$), the blades bend more severely near the base producing a smaller radius of curvature than that implied by the scale $|d^2\theta/ds^2| \sim 1/l^2$ used in Eq. 5, and so the restoring force due to blade stiffness is larger than that implied by the scale $EI(1/l)^2$. For bent postures, the effective length, l_e, captures the magnitude of the restoring force more accurately because it reflects the length over which the blade is actually bending, leading to $EI(|d^2\theta/ds^2|) \sim EI(1/l_e)^2$. Since the restoring force due to stiffness and the drag force must balance in the reconfigured state, we have $EI(1/l_e)^2 \sim (1/2)\rho C_D b l_e U^2$. Expressing this balance in dimensionless form (*see* Eq. 8), we see that the effective length scales as $(l_e/l) \sim Ca^{-1/3}$.

We now discuss the general case, where blade buoyancy and stiffness are both important. As before, we solve Eq. 6 numerically using an iterative shooting method. The four curves in Fig. 2c show effective lengths for the zero-buoyancy case described above, $B = 0$ (bold black line), along with the cases $B = 10$ (fine black line), 50 (bold gray line) and 100 (fine gray line). Comparing these four curves indicates that the addition of buoyancy delays the onset of blade

reconfiguration relative to the zero-buoyancy case (Fig. 2c), i.e., the blades remain upright at higher velocities. For the zero-buoyancy case, the effective length is approximately equal to the blade length, $(l_e/l) \approx 1$, for $Ca < O(1)$. For $B > 1$, the effective length is approximately equal to the blade length as long as the drag force scale does not exceed the buoyancy force scale, $(B^{-1}Ca) < O(1)$, or $Ca < O(B)$. As an example, for $B = 100$, $l_e/l \approx 1$ for $Ca < O(100)$ (Fig. 2c). Above these thresholds, the blades are pushed over by the flow and the effective length decreases.

If the hydrodynamic forcing becomes significantly larger than blade buoyancy, $(B^{-1}Ca) >> 1$, blade stiffness becomes the dominant restoring mechanism. Specifically, all the curves collapse onto the scaling law developed above, $(l_e/l) \sim Ca^{-1/3}$, and the effective length becomes independent of the buoyancy parameter, B. This is illustrated by the predicted blade postures for $Ca = 1000$ (Fig. 2c, right-most inset). Close to the base, blade posture is very similar for all four values of the buoyancy parameter, indicating that the curvature close to the bed is set purely by a balance between drag and the restoring force due to blade stiffness. The effect of buoyancy only becomes apparent closer to the top of the blades; the more buoyant blades are raised a bit higher in the water. However, given the near-horizontal orientations, the top of the blades do not generate significant drag. The majority of the drag is generated very close to the base, where the blades are clamped and remain vertical due to blade stiffness. As a result, blade buoyancy does not significantly affect the drag generated, and the effective length, which characterizes drag, becomes independent of the buoyancy parameter.

Laboratory experiments

To validate the model developed above, we conducted laboratory experiments measuring drag and blade posture for model blades designed to be dynamically similar to seagrasses. Due to variations in material properties, morphology and flow conditions, the buoyancy parameter and

Cauchy number vary considerably in natural systems. For example, the typical density of the seagrass *Zostera marina* varies in the range 700 – 900 kg m^{-3} (Fonseca 1998; Abdelrhman 2007; Fonseca et al. 2007), so that $\Delta\rho \approx 125 – 325$ kg m^{-3} (the density of seawater is assumed to be 1025 kg m^{-3}), and the range of reported values for the elastic modulus is $E \approx 0.4 – 2.4$ GPa (Bradley and Houser 2009). *Zostera marina* blades can also vary greatly in length with observations ranging from $l \approx 15 – 200$ cm (Ghisalberti and Nepf 2002). Using a more typical blade length range of $l = 30 – 60$ cm, and assuming the blade width and thickness are $b = 0.8$ cm and $t = 0.35$ mm (Luhar et al. 2010), we estimate that the buoyancy parameter (Eq. 7) ranges between $B \approx 1 – 170$. For a typical velocity range of $U = 5 – 50$ cm s^{-1}, we estimate the Cauchy number (Eq. 8) ranges from $Ca \approx 10 – 40{,}000$.

To span the estimated range for the buoyancy parameter, we constructed model blades from two different materials, silicon foam ($E = 500$ kPa; $\Delta\rho = 330$ kg m^{-3}; $t = 1.9$ mm) and high-density polyethylene (HDPE, $E = 0.93$ GPa; $\Delta\rho = 50$ kg m^{-3}; $t = 0.4$ mm). We tested model blades of five different lengths ranging from $l = 5$ cm to $l = 25$ cm in 5 cm-increments. The blade width was $b = 1.0$ cm in all cases. For the foam blades, the buoyancy parameter ranged from $B = 2.7$ for the 5 cm-long blades to $B = 340$ for the 25 cm-long blades (Table 1). For the HDPE blades, the buoyancy parameter ranged from $B = 5\times10^{-3}$ for the 5 cm-long blades to $B = 0.62$ for the 25 cm-long blades (Table 1). In general, the foam blades represented buoyancy-dominated cases, while the HDPE blades represented stiffness-dominated cases. All the model blades were subjected to eight different flow speeds, ranging from $U = 3.6$ cm s^{-1} to $U = 32$ cm s^{-1}. The maximum value of the Cauchy number tested was $Ca = 5500$ for the foam blades, and $Ca = 320$ for the HDPE blades. Note that because the model blades resemble flat plates, these values for the Cauchy number have been calculated based on the drag coefficient for long, flat plates

298 perpendicular to the flow, C_D = 1.95 (Vogel 1994). Table 1 lists the buoyancy parameter and the
299 Cauchy number for all eighty test cases.

300 For flow speeds smaller than U = 15 cm s^{-1}, the experiments were performed in a 24 m-
301 long, 38 cm-wide and 60 cm-deep re-circulating flume. For flow speeds greater than U = 15 cm
302 s^{-1}, the experiments were carried out in a 28 m-long, 76 cm-wide and 90 cm-deep re-circulating
303 flume. Both flumes had glass sidewalls. A schematic of the experimental set-up is shown in Fig.
304 3. At every flow speed, the horizontal drag force, F_x, acting on a single model blade of each
305 length tested was measured using a submersible s-beam load cell (Futek LSB210). The
306 measurements were logged to a computer using a bridge completion and data acquisition module
307 (National Instruments NI-USB 9237). Based on a calibration with known weights performed
308 prior to the experiments, the resolution of the load cell was 0.001 N and the accuracy was 10%.
309 Two separate calibrations showed that the load cell responded linearly over the range 0 – 0.015
310 N (r^2 = 1.00, n = 13), and over the range 0 – 0.042 N (r^2 = 1.00, n = 10).

311 To ensure that the flow did not interfere with the force measurement apparatus, the load
312 cell was housed inside a trapezoidal, acrylic box of length 192 cm and height 12.7 cm, as shown
313 in Fig. 3. In all cases, the total water depth was 42.7 cm, so that the depth of the water above the
314 acrylic box was 30 cm. The load cell was fixed to the top surface of the box, midway along the
315 length of the box. A cylindrical, stainless steel blade holder, which protruded through a hole of
316 diameter 1.25 cm, was used to attach the model blades to the load sensor (Fig. 3). The blade
317 holder extended 4 cm above the top of the box. As a result, the model blades were positioned
318 above the bottom boundary layer, ensuring a uniform flow speed over the length of the blade.
319 Prior to the experiments, we measured vertical profiles of velocity above the acrylic box using an
320 Acoustic Doppler Velocimeter (ADV, Nortek Vectrino) for all eight flow speeds. We measured

the velocity profiles midway along the box at a vertical resolution of 1 cm. At each measurement location, 4-min records were obtained at 25 Hz. The vertical profiles, shown in Fig. 3, confirm that the horizontal flow speed varied by less than 5% above blade holder. Note that the velocity values listed in this paper denote the mean horizontal flow speed above the blade holder.

Force measurements were made for a period of 4 min at a sampling rate of 2 kHz (i.e., 480,000 samples). The drag force was calculated based on the arithmetic mean of all the samples. We also measured the force generated by the blade holder alone for each of the eight flow speeds tested. In order to estimate the drag force generated by the blades alone, the drag generated by the blade holder was subtracted from the total drag (i.e., blade holder and blade). In addition to measuring the drag force, we also photographed the model blades for each flow speed using a digital still camera (Nikon D60). Multiple photographs were taken for each test case to account for any short-term fluctuations in blade posture.

Results

Model blades

Figure 4 shows force measurements (Fig. 4a,b, symbols) and observed blade postures (Fig. 4c-f) for the shortest (5 cm) and longest (25 cm) model blades tested. Vortex-induced vibrations of the HDPE blades were observed at velocities greater than 20 cm s^{-1}. However, the standard deviations from the mean measured forces were smaller than 10% in all cases. Hence, the errorbars in Fig. 4a,b reflect the 10% accuracy of the load cell. Model predictions for drag (Fig. 4a,b, lines) and blade posture (Fig. 4c-f, white curves) are also shown. The model force predictions agree with the observations for all but the shortest HDPE blade. For the 5 cm HDPE blade, the horizontal force, F_x, is over-predicted by the model (Fig. 4a, black squares and line). This over-prediction may be due to the fact that for flat plates with small length-to-width ratios,

344 pressure recovery near the tip leads to a drag coefficient that is lower than the value assumed
345 here, $C_D = 1.95$ (Vogel 1994).

346 When the Cauchy number is small, $Ca \leq 2.5$ (Table 1), the blades do not reconfigure
347 significantly and the standard quadratic drag law applies. For example, the 5 cm HDPE blade
348 ($Ca \leq 2.5$ for all flow speeds, Table 1) remained near-vertical even at the highest velocity tested
349 (Fig. 4c), and the measured horizontal forces were approximately proportional to the square of
350 velocity (Fig. 4a). Specifically, the horizontal force increased with velocity as $F_x \propto U^a$, with $a =$
351 1.86±0.05. As the Cauchy number increases so that $Ca >> 1$, reconfiguration becomes significant
352 and the quadratic law overestimates drag. As an example, the 25 cm HDPE blade exhibited some
353 reconfiguration over the entire range of velocities tested here ($Ca = 3.9 – 320$, Table 1). The
354 blade remained vertical near the clamped base, but blade curvature increased with increasing
355 velocity (Fig. 4e). This flow-induced streamlining led to a near-linear relationship between the
356 measured drag force and velocity (Fig. 4a). Specifically, $F_x \propto U^a$ with $a = 1.31 \pm 0.10$, in
357 agreement with the predicted scaling law, $F_x \propto U^{4/3}$. Note that, because of reconfiguration, the
358 drag generated by the 25 cm HDPE blade was comparable to the drag generated by the 5 cm
359 blade for velocities greater than 25 cm s^{-1} (Fig. 4a). This is because reconfiguration reduces drag
360 both by reducing frontal area and by producing more streamlined shapes. For $U = 32$ cm s^{-1}, the
361 25 cm HDPE blade had a larger frontal area than the 5 cm blade (*see* Fig. 4c,e). However, the
362 drag generated by the longer blade was reduced because it was pushed over into a more
363 streamlined posture compared to the upright shorter blade.

364 For the 25 cm foam blade ($B = 340$, Table 1), the reconfiguration response resembled the
365 zero-stiffness limiting case, with a nearly constant θ along most of the blade length. However,
366 curvature is observed at the bed because the blade is clamped, not pinned, as assumed by the

model for the zero-stiffness case. Note that the curvature occurs over a much shorter length scale (i.e., smaller radius of curvature) than that observed for the stiffer HDPE blade (*see* Fig. 4e,f). This reinforces the idea that, even for buoyant blades with $B >> 1$, stiffness plays a role in determining posture near the bed. The observed postures for the foam blades are slightly more upright compared to the model predictions for $U = 16$ cm s^{-1} (Fig. 4d, f). This discrepancy may be due to the uncertainty in B caused by variations in the foam density (Table 1).

For velocities between 5 cm s^{-1} and 20 cm s^{-1}, the drag generated by the 25 cm foam blades (Fig. 4b, gray circles) increased sub-linearly with velocity i.e., $F_x \propto U^a$ with $a =$ 0.69±0.22. This sub-linear relationship between drag and velocity is characteristic of a buoyancy-dominated response, as discussed earlier. For velocities greater than $U \approx 20$ cm s^{-1}, however, the drag-velocity behavior of the 25 cm foam blade converged with that of the 5 cm foam blade, for which $a = 1.54$±0.20 (Fig. 4b, black squares). This exponent agrees, within uncertainty, with the value 4/3 predicted for stiffness-dominated regimes, which is expected for $B^{-1}Ca >$ O(1). Indeed, for $U \approx 20$ cm s^{-1}, $B^{-1}Ca \approx 6$ (Table 1). Hence, we see that a single blade can transition between the buoyancy-dominated and stiffness-dominated regimes with increasing velocity. When the drag force scale exceeds blade buoyancy, $B^{-1}Ca >$ O(1), blade stiffness becomes the dominant restoring mechanism, and the predicted scaling law $F_x \propto U^{4/3}$ applies, even if the value of B (>> 1) implies that buoyancy should dominate.

The force measurements for the foam blades also suggest that when $B^{-1}Ca >$ O(1), drag becomes independent of blade length. For $U >$ 20 cm s^{-1}, the measured forces for both the 5 cm- and 25 cm foam blades agree within uncertainty (Fig. 4b). At $U \approx 20$ cm s^{-1}, $B^{-1}Ca \approx 6$ for both the 5 cm and 25 cm foam blades (*see* Table 1). Above this threshold velocity, reconfiguration is stiffness-dominated for both foam blades and the effective length scales as $l_e/l \sim Ca^{-1/3}$. Since the

Cauchy number is proportional to l^3 (Eq. 8), this scaling implies that the effective length becomes independent of the blade length, $l_e \sim l\,(Ca^{-1/3}) \propto l^0$, and hence, so does the drag force.

Consistent with the data shown in Fig. 4, the model is able to accurately predict the effective blade length, l_e/l, for all eighty test cases (Fig. 5). The measured effective lengths were calculated from the measured forces, F_x, using the relation: $(l_e/l) = F_x/(1/2\rho C_D b l U^2)$. The effective lengths for all the HDPE blades fall onto a single curve (Fig. 5a), which is similar to the zero-buoyancy case shown in Fig. 2b. This result suggests that for $B < 1$ (*see* Table 1), blade stiffness is the dominant restoring mechanism and the effect of buoyancy on reconfiguration may be neglected. Further, in agreement with model predictions, the data suggest the following scaling relationships at the stiff and flexible limits: $(l_e/l) \sim Ca^{\alpha}$, with $\alpha = -0.07 \pm 0.03$ for $Ca < 2$, and $\alpha = -0.41 \pm 0.06$ for $Ca > 10$.

In contrast, the effective lengths for the foam blades of different length follow distinct curves (Fig. 5b) that depend on the value of the buoyancy parameter (*see* Table 1), confirming the model prediction (Fig. 5b, solid lines) that blade buoyancy delays the onset of reconfiguration. However, all five curves seem to collapse together for $B^{-1}Ca > O(1)$ (*see* Fig. 5b, $Ca > 1000$), again indicating that once the hydrodynamic forcing exceeds blade buoyancy, blade stiffness becomes the dominant restoring mechanism, and so blade stiffness may not be neglected even if $B >> 1$. Recall that even at the highest B, curvature is observed near the bed (Fig. 4f), indicating that stiffness must influence posture.

Note that the model predictions described in this section were based on the known blade properties, flow speed and the drag coefficient for flat plates. No empirical fitting parameters were used. Agreement between the experimental observations and the predictions therefore confirms that the model effectively captures the physics underlying the flow-induced

413 reconfiguration of buoyant, flexible blades. Of course, the experiments were designed to fit the
414 simplifying assumptions made to develop the model. For example, the model blades had a
415 constant, rectangular cross-section, and the blade material properties did not vary over the blade
416 length. The flow speed was also constant over the length of the blade. Below, we show that the
417 model developed here is also able to predict drag and posture for real aquatic vegetation in flow,
418 where some of these simplifying assumptions break down.

419 *Real aquatic vegetation*

420 Abdelrhman (2007) photographed *Zostera marina* blades exposed to three different flow
421 speeds, $U = 6$ cm s^{-1}, 12 cm s^{-1}, and 14 cm s^{-1}. The model described here accurately predicts the
422 observed postures (Fig. 6). As mentioned above, the geometric and material properties for
423 *Zostera marina* blades vary significantly in natural systems. To arrive at our estimates for blade
424 posture, we assumed that the blade width and thickness were $b = 0.8$ cm and $t = 0.35$ mm,
425 respectively (Luhar et al. 2010). As before, we assumed that the drag coefficient was identical to
426 that for flat-plates, $C_D = 1.95$. Abdelrhman (2007) reported that the blade density was 700 kg m^{-3}
427 , so that $\Delta\rho = 325$ kg m^{-3}, and the blade length was $l = 40$ cm. We estimated blade postures for
428 two different values of the elastic modulus, $E = 0.4$ GPa and $E = 2.4$ GPa, corresponding to the
429 minimum and maximum values reported by Bradley and Houser (2009). The more upright
430 predicted posture (Fig. 6) corresponds to the higher elastic modulus, $E = 2.4$ GPa.

431 Abdelrhman (2007) also developed a coupled flow-structure model to predict seagrass
432 posture in flow, which was able to predict the deflected height of the seagrass reasonably well.
433 However, the model developed by Abdelrhman (2007), assumed that blade stiffness was
434 negligible, and that posture was set by a balance between hydrodynamic forces (drag, lift and
435 skin friction) and buoyancy. Unsurprisingly, the blade posture predictions made by this model

436 resemble the postures shown in Fig. 2a for the zero-stiffness case (i.e., pin-joint at the bed and a
437 constant angle θ). Clearly, this is not consistent with the images shown in Fig. 6, which indicate
438 that the seagrasses remain upright close to the bed. The images also show that an increase in
439 velocity leads to an increase in curvature near the bed. These observations suggest that blade
440 stiffness is important.

441 Fonseca and Kenworthy (1987) observed the deflected height, h/l, for three different
442 species of seagrass exposed to flow: *Thalassia testudinum*, *Halodule wrightii*, and *Zostera*
443 *marina*. Figure 7 compares the observations (symbols) with model predictions (lines, Eq. 10).
444 Table 2 lists the reported blade properties for each species of seagrass that were used here to
445 predict deflected height. The natural variability in seagrass blade properties is reflected in the
446 upper- and lower-bound predictions shown as dashed lines. The upper- and lower-bound
447 predictions correspond to the stiffest (lowest B, Table 2) and most flexible (highest B, Table 2)
448 cases, respectively. In general, the observations lie within the limits predicted by the model.
449 However, there are some discrepancies. Figure 7a shows that the observed deflected height for
450 *Thalassia testudinum* lies closer to the upper-limit predicted by the model. Also, some outliers
451 appear above the upper-limit. These results indicate that the assumed blade properties
452 underestimate blade stiffness or blade buoyancy for the specific population of *Thalassia*
453 *testudinum* studied by Fonseca and Kenworthy (1987). For instance, the elastic modulus may
454 have been greater than the assumed value, $E = 2.4$ GPa. Note also that we do not consider any
455 variations in seagrass buoyancy, or blade thickness. Seagrass blade buoyancy can change over
456 time and in response to flow conditions (Abdelrhman 2007), and so the assumed density
457 difference between the blades and the water ($\Delta\rho = 85$ kg m^{-3}), could be an underestimate.
458 Similarly, the blade stiffness is proportional to the cube of blade thickness, $I \propto t^3$, and so even a

459 relatively small increase in blade thickness could lead to significantly stiffer blades. Finally,
460 previous studies (Fonseca et al. 1982) suggest that the maximum bending for *Zostera marina* is
461 achieved at a velocity of ~50 cm s^{-1}. The predictions shown in Fig. 7c are consistent with this
462 observation.

463 Stewart (2006) measured the forces acting on the marine macroalga *Turbinaria ornata*
464 exposed to currents. This macroalga consists of a central stipe, or stem, that is covered with
465 blades and pneumatocysts along part of its length. Stewart (2006) noted that populations of this
466 macroalga in sheltered, backreef habitats had buoyant pneumatocysts, while populations in
467 wave-exposed, forereef habitats lacked pneumatocysts, or that the pneumatocysts were very
468 small and non-buoyant. Instead, algae from the forereef sites had shorter, thicker stipes. To test
469 how these variations in morphology affected drag, Stewart (2006) measured the forces acting on
470 algae samples obtained from an exposed, forereef site, and a sheltered backreef, site, for
471 velocities ranging from $U = 32$ cm s^{-1} to $U = 75$ cm s^{-1}. The force measurements were used to
472 estimate the drag coefficient in the reconfigured state, C_D*, using the quadratic drag law, $C_D^* = F_x/(1/2\rho A U^2)$, where A is the planar surface area for the algae in an un-deflected state. Recall that
474 the effective length is defined as $(l_e/l) = F_x/(1/2\rho C_D A U^2)$. We calculated the effective length from
475 the reported values of C_D* by combining the above relations, leading to $(l_e/l) = C_D^*/C_D$. The data
476 shown in Stewart (2006) suggest that the drag coefficient was $C_D \approx 2$ at the limit when the
477 macroalgae remained upright in the water. Hence, we assumed $C_D = 1.95$, as before.

478 To arrive at model predictions for this morphologically complex macroalga, we
479 calculated the buoyancy parameter as $B = F_B l^2/EI$ (c.f. Eq. 7), where F_B is the total buoyancy of
480 each alga, l is the total stipe length, E is the elastic modulus and $I = \pi r^4/4$ is the second moment
481 of area for the stipe of radius r. Similarly, we calculated the Cauchy number based on the

relation $Ca = (1/2)\rho C_D A U^2 l^2/(EI)$ (c.f. Eq. 8). The vegetation parameters used to estimate B and Ca were either reported by Stewart (2006), or estimated from values given in that paper. We repeat them in Table 3 for convenience. The buoyancy parameters were $B = 15$ and $B = -0.56$ for the backreef and forereef samples, respectively. The negative value for the buoyancy parameter indicates that the forereef algae were denser than water.

Despite the more complex vegetation morphology, agreement between the observed and predicted values for effective length is very good (Fig. 8). The shorter, stiffer forereef samples remained more upright over the range of velocities tested by Stewart (2006), and therefore had higher effective lengths. In contrast, the longer, more flexible backreef samples were pushed over by the flow, leading to lower effective lengths. The flow speeds tested by Stewart (2006) were higher than those recorded in the sheltered, backreef location but lower than those for the exposed, forereef site. The ranges of field conditions reported by Stewart (2006) are marked by shaded regions in Fig. 8. For conditions characteristic of the backreef site, the hydrodynamic forcing and buoyancy are comparable, $B^{-1}Ca \approx \mathrm{O}(1)$, and so the model predicts that the buoyant, backreef algae are likely to remain upright. However, for conditions characteristic of the forereef site, the Cauchy number is large, $Ca > \mathrm{O}(10)$, and so the model predicts significant reconfiguration for the forereef algae. Below, we briefly discuss the possible ecological implications of these results.

Discussion

By considering the differences in the reconfiguration response for buoyancy- and stiffness-dominated cases, we can start to address how selective pressures may produce differences in vegetation morphology across different flow environments, such as those observed by Stewart (2006). As described above, Stewart (2006) observed that populations of the

505 macroalga *Turbinaria ornata* in sheltered, backreef habitats had buoyant pneumatocysts, while
506 populations in exposed, forereef habitats lacked pneumatocysts, or had pneumatocysts that were
507 small and non-buoyant. This variation can perhaps be explained based on the limited nature of
508 the restoring force due to buoyancy. Stewart (2004) suggests that an upright posture can benefit
509 benthic vegetation both by increasing light availability and by enhancing nutrient and oxygen
510 transfer. If the primary purpose of the buoyant pneumatocysts is to help maintain an upright
511 posture, investment in pneumatocysts would only be worthwhile if the additional buoyancy has a
512 significant effect on posture. This is only possible if the drag force scale is smaller than the
513 buoyancy force, $B^{-1}Ca \leq O(1)$. The material and geometric properties listed in Table 3 suggest
514 that this is unlikely to be the case for these macroalgae at velocities typical of the forereef site (U
515 ≈ 100 cm s^{-1}, Fig. 8). Even if the forereef samples were as buoyant as the backreef samples, so
516 that $F_B = 23$ mN (instead of -10 mN, Table 3), the buoyancy parameter would be $B \approx 1.4$ (instead
517 of $B = -0.6$), while the Cauchy number would be $Ca \approx 37$ for $U = 100$ cm s^{-1}, leading to $B^{-1}Ca$
518 $>> 1$. As a result, the additional buoyancy afforded by the pneumatocysts would have little effect
519 on posture. In contrast, for velocities typical of the sheltered, backreef site ($U \approx 15$ cm s^{-1}, Fig.
520 8), the Cauchy number is $Ca \approx 17$, which is comparable to the value of the buoyancy parameter
521 for the backreef samples, $B = 15$. In this case, since $B^{-1}Ca \sim O(1)$, investment in the
522 pneumatocysts may be worthwhile because buoyancy can help maintain an upright posture.
523 We must stress that the above discussion is presented primarily as a starting point for
524 further study. A more complete analysis of the ecological trade-offs associated with allocating
525 resources towards pneumatocysts rather than stem or leaf tissue needs to account for many other
526 factors in addition to posture in the water column. A deeper understanding of the energetic costs
527 involved is necessary. The effect of this allocation on photosynthetic performance and

susceptibility to breakage must also be considered. Further, *Turbinaria ornata* grows in wave-dominated environments and so any discussion of hydrodynamic performance must take into account the work of Denny and colleagues, who have studied the interaction between buoyant, flexible organisms and waves extensively (Denny et al. 1997; Denny et al. 1998; Denny and Gaylord 2002).

A number of assumptions were made to yield the governing Eq. 6 for blade posture. The assumption of a rectangular beam cross-section is reasonable for seagrasses (Folkard 2005; Fonseca et al. 2007) but the cross-section and material properties can vary along a real blade (Fonseca et al. 2007; Bradley and Houser 2009). In addition, the flow speed is likely to vary along the blade. We can account for spatial variations in vegetation properties (E, I, $\Delta\rho$, b, t, C_D) and velocity (U) by reverting Eq. 5 to a more general form:

$$\frac{d}{ds}\left(-EI\frac{d\theta}{ds}\right)\bigg|_{s*} + \sin\theta * \int_{s*}^{l} \Delta\rho g b t ds = \int_{s*}^{l} \frac{1}{2}\rho C_D b U^2 \cos^2\theta \cos(\theta - \theta *) ds \qquad (14)$$

Eq. 14 can then be made dimensionless as before. However, because the blade material properties and flow vary along the blade length, the buoyancy parameter (Eq. 7) and Cauchy number (Eq. 8) must be defined using characteristic values (e.g., an average) for these quantities. Unfortunately, the spatial variation of material properties remains poorly characterized, and the flow structure depends on both blade posture and canopy density (Luhar et al. 2008; Dijkstra and Uittenbogaard 2010; Luhar et al. 2010). As a result, an extension of the model to include these variations introduces additional uncertainty.

Depth-uniform flow is a reasonable assumption only for individual plants (or very sparse canopies) over smooth beds such that vegetation does not significantly affect the flow, and the height of the bottom boundary layer is small compared to the height of the vegetation. However, the presence of neighboring blades can change the flow structure, which can affect the

551 reconfiguration response. To explore this point, we compare the reconfiguration response for a
552 depth-uniform flow of velocity $U(0 \le z \le h) = u$ with that for the two representative velocity
553 profiles shown in Fig. 9a. For sparse vegetation canopies, the velocity profile approaches that of
554 a rough, turbulent boundary layer (fig. 1 in Luhar et al. 2008). As an abstraction of this case, we
555 consider a profile where the velocity, $U(z)$, increases linearly from 0 to $2u$ over the canopy
556 height, h ('sparse canopy', Fig. 9a). For dense canopies, the velocity profile resembles a shear
557 layer with an inflection point near the top of the canopy (fig. 1 in Luhar et al. 2008). As an
558 abstraction of this case, we consider the velocity in the lower half of the canopy to be constant,
559 $U(z < h/2) = 2u/3$, and in the upper half of the canopy ($h/2 \le z \le h$) to be linearly increasing from
560 $2u/3$ to $2u$ ('dense canopy', Fig. 9a). We solve the governing Eq. 14 for these velocity profiles
561 using an iterative shooting method for two different values of the buoyancy parameter, $B = 0$ and
562 $B = 100$. Note that for all three velocity profiles, the average velocity over the canopy height is u.
563 Hence, we calculate the Cauchy number (Ca, Eq. 8) and effective length (l_e/l, Eq. 9) using u as
564 the velocity scale.

565 For both values of B, the predicted deflected canopy heights (h/l, Fig. 9b) for each of the
566 three velocity profiles are nearly identical for $Ca = 1$ to 1000. The maximum absolute difference
567 in h/l is 0.04 over this range, suggesting that the simple depth-uniform model developed here
568 may be used to reasonably predict h/l for field conditions as long as the canopy-averaged
569 velocity is used to calculate Ca. The effective lengths (l_e/l, Fig. 9c) for the three velocity cases
570 also show similar trends. However, there are some differences. For $Ca = 1$, the effective lengths
571 are higher for the sparse and dense canopy cases compared to the depth-uniform case. At $Ca = 1$,
572 the plants remain nearly upright and drag is generated along the entire canopy height. Since drag
573 per unit length is proportional to $U(z)^2$ and the canopy-average of $U(z)^2$ is greater than u^2 for both

574 the sparse and dense canopy cases, the effective length is larger. In contrast, for Ca = 1000, the
575 depth uniform case has the largest effective length. At Ca = 1000, the vegetation is pushed over
576 so far that the drag is generated primarily in the lower part of the canopy. Since $U(z) < u$ in the
577 lower part of the canopy for the sparse and dense canopy cases (Fig. 9a), the drag generated for
578 these cases is lower than that for the depth-uniform case.

579 While seagrass blades have relatively simple, strap-like morphologies, other marine and
580 freshwater macrophytes can have more complex forms. For example, many marine (Stewart
581 2006) and freshwater (Sand-Jensen 2003) macrophytes consist of a stem covered with leaf-like
582 structures and buoyant, gas-filled pneumatocysts. The *Turbinaria ornata* case study described
583 above (Stewart 2006) shows that the model developed here remains applicable for such
584 macrophytes as long as appropriate changes are made to the buoyancy parameter and Cauchy
585 number. Specifically, the restoring force due to vegetation stiffness should be scaled on the
586 properties of the central structural element - the stem, while the drag force should be scaled on
587 the planar surface area of the vegetation to account for the contribution of the leaves. The
588 buoyancy parameter should be scaled on the net buoyancy force generated by the gas-filled
589 pneumatocysts. Other aquatic macrophytes such as kelp have drag- and buoyancy-generating
590 structures concentrated near the top of the stem. For such cases, the spatial distribution of drag
591 and buoyancy in the governing equation (Eq. 14) must be modified.

592 The model developed here only considers form drag. As the blades assume more
593 streamlined postures, skin friction can become important. To assess when skin friction becomes
594 significant, we consider the limit at which skin friction equals 10% of the horizontal form drag,
595 $F_x = (1/2)\rho C_D b l_e U^2$. The skin friction force on a horizontal beam of length l and width b is F_f =

596 $(1/2)\rho C_f b l U^2$ where C_f is the skin friction coefficient (Kundu and Cohen 2004). A comparison of
597 F_f and F_x shows that skin friction becomes important when the effective length is

598 $$\frac{l_e}{l} \le \frac{10 C_f}{C_D} \qquad (15)$$

599 Note that this limit is conservative since it compares form drag in the reconfigured state with
600 skin friction on the entire blade length. As before, the drag coefficient for flat plates normal to
601 flow is $C_D = 1.95$. For horizontal plates with laminar boundary layers, the skin friction
602 coefficient is $C_f = 1.33\ Re^{-1/2}$, where $Re = Ul/\nu$ is the Reynolds number based on plate length, l
603 (Kundu and Cohen 2004). Substituting these expressions for C_D and C_f into Eq. 15, we see that
604 skin friction becomes important as the effective blade length decreases below $(l_e/l) < 6.8\ Re^{-1/2}$.
605 However, this relationship breaks down if the boundary layer on the blades becomes turbulent.
606 The transition to a turbulent boundary layer depends both on flow properties and surface
607 roughness. For relatively smooth surfaces, this transition is likely to occur as the Reynolds
608 number increases above $Re \approx 10^5$ (Kundu and Cohen 2004). Using $l = 30$ cm as a typical blade
609 length, the Reynolds number approaches this limit for a flow speed of $U \approx 30$ cm s^{-1}. For a range
610 of flow speeds $U = 3 - 300$ cm s^{-1}, the Reynolds number is $Re = 10^4 - 10^6$, so that the skin
611 friction coefficient for laminar boundary layers is $C_f \approx 0.001 - 0.01$. For turbulent boundary
612 layers, C_f is also expected to be of $O(0.001 - 0.01)$ (Kundu and Cohen 2004). For $C_f \approx 0.01$, a
613 conservative value, Eq. 15 suggests that skin friction is important for $(l_e/l) < 0.05$. However, note
614 that smooth surfaces are rare in the field. Even relatively smooth seagrasses are often covered by
615 epiphytes, which are likely to increase skin friction.

616 The model and results obtained in this study can inform the debate about the how to best
617 characterize reconfiguration and drag for flexible macrophytes (Green 2005; Sukhodolov 2005;
618 Statzner et al. 2006). Using the quadratic law, the drag force is usually expressed as $F_x =$

619 $(1/2)\rho C_D A U^2$. As discussed in Statzner et al. (2006), the effects of reconfiguration may be
620 captured by changing either the drag coefficient, C_D, or the characteristic area, A, or by changing
621 both. One option is to use the frontal area of the reconfigured vegetation as the characteristic area
622 scale (Statzner et al. 2006). However, as discussed above, reconfiguration reduces drag through
623 two mechanisms: reduced frontal area and more streamlined shapes. As a result, using the frontal
624 area would additionally require changing the drag coefficient to account for the more streamlined
625 shapes. With two changing parameters, comparing results across studies becomes more difficult.
626 Instead, we suggest the use of an effective length, l_e, so that the characteristic area is $A = bl_e$,
627 where b is a characteristic width. The advantage of this approach is that it allows us to account
628 for the two distinct physical phenomena that can affect drag: Reynolds number effects can be
629 accounted for via the drag coefficient, C_D, and vegetation reconfiguration may be accounted for
630 via the effective length, l_e, which is governed by the Cauchy number, Ca, and buoyancy
631 parameter, B. The drag would then be estimated as $F_x = (1/2)\rho C_D b l_e U^2$, using the drag
632 coefficient, C_D, for a rigid, upright blade. As it is not practical in all cases to develop a model
633 similar to that described here, as an approximation, we suggest the following physically-
634 motivated empirical relationship for effective length:

635 $$\frac{l_e}{l} = 1 - \frac{\left(1 - 0.9Ca^{-1/3}\right)}{1 + Ca^{-3/2}(8 + B^{3/2})} \qquad (16)$$

636 The functional form of Eq. 16 was chosen to match model predictions for the zero-stiffness (Fig.
637 2a) and zero-buoyancy (Fig. 2b) cases. Eq. 16 reduces to $(l_e/l) \approx 1$ when the drag force scale is
638 smaller than either the restoring force due to buoyancy ($B^{-1}Ca \ll 1$) or the restoring force due to
639 stiffness ($Ca \ll 1$). For the zero-stiffness case Eq. 16 yields $(l_e/l) \sim (B^{-1}Ca)^{-3/2}$ as $B^{-1}Ca \gg 1$ (*see*
640 Fig. 2a) and similarly, for the zero-buoyancy case, Eq. 16 simplifies to the predicted scaling (l_e/l)
641 $\sim Ca^{-1/3}$ for $Ca \gg 1$ (*see* Fig. 2b). Figure 10 shows that this empirical relationship (dashed lines)

642 follows model predictions (solid lines) extremely well for the general case. The maximum
643 absolute difference between the two predictions for effective length, (l_e/l), is ~0.03 over the
644 range of parameters shown (B = 0 to 100, Ca = 0.1 to 10^4).

645 The predicted scaling law for effective length, (l_e/l) ~ $Ca^{-1/3}$, can also be interpreted in
646 terms of the Vogel exponent, often reported as a measure of reconfiguration (Vogel 1994). The
647 Vogel exponent, γ, quantifies deviations from the quadratic drag law by assuming the following
648 relationship between drag and velocity: $F_x \propto U^{2+\gamma}$. The quadratic drag law holds for rigid, upright
649 bodies at high Reynolds number, for which $\gamma \approx 0$. However, because flexible bodies are pushed
650 over by the flow, the drag is reduced, leading to $\gamma < 0$. Using the predicted relationship, (l_e/l) ~
651 $Ca^{-1/3}$, the drag force is proportional to $U^{4/3}$, which leads to a Vogel exponent of $\gamma = -2/3$.
652 Consistent with this prediction, the observations made by Boller and Carrington (2006) indicate
653 that $\gamma \approx -0.60$ for the intertidal macro alga *Chondrus crispus*. For the terrestrial giant reed
654 *Arundo donax*, Harder et al. (2004) observed that the Vogel exponent transitions from a value of
655 $\gamma = -0.12$ for velocities smaller than U = 1.5 m s^{-1}, to $\gamma = -0.71$ for velocities greater than U =
656 1.5 m s^{-1}. The low-velocity condition is consistent with a quadratic drag law ($\gamma = 0$), implying
657 that these flows do not induce reconfiguration. However, for U > 1.5 m s^{-1}, the observed
658 coefficient is consistent with the stiffness dominated reconfiguration ($\gamma = -2/3$). The
659 observations described above suggest that the predicted scaling law for stiffness-dominated
660 reconfiguration, $F_x \propto U^{4/3}$, holds for many systems. Note that for buoyancy-dominated systems
661 ($B >> 1$), the drag force can increase sub-linearly with velocity (Fig. 4b), so that $\gamma < -1$.
662 However, once the drag scale exceeds blade buoyancy, $B^{-1}Ca$ > O(1), the predicted scaling law
663 for effective length, (l_e/l) ~ $Ca^{-1/3}$, applies again and the Vogel exponent reverts to $\gamma = -2/3$.

This study shows that a simple model balancing the effects of hydrodynamic drag with the restoring forces due to vegetation stiffness and buoyancy can successfully predict posture and drag for both model and natural aquatic vegetation. As a result, we suggest that future work considering the interaction between flow and flexible vegetation should be framed in terms of the two dimensionless parameters that represent the ratios of these three forces: the Cauchy number (*Ca,* Eq. 8) and the buoyancy parameter (*B*, Eq. 7). The use of this convention has not only been successful in the past (Nikora 2010), it also makes a quantitative comparison of reconfiguration possible across vegetation species and hydrodynamic conditions. At the same time, some caution is required when using these dimensionless parameters to guide theory and experiment. It is tempting to disregard vegetation stiffness for cases where $B >> 1$. However, this study clearly demonstrates that even for $B >> 1$, vegetation stiffness can be important once hydrodynamic drag exceeds vegetation buoyancy, i.e., $B^{-1}Ca > O(1)$.

676 **References**

677 Abdelrhman, M. A. 2007. Modeling coupling between eelgrass Zostera marina and water flow.
678 Mar. Ecol. -Prog. Ser. **338:** 81-96.

679 Alben, S., M. Shelley, and J. Zhang. 2002. Drag reduction through self-similar bending of a
680 flexible body. Nature **420:** 479-481, doi:10.1038/nature01232

681 Alben, S., M. Shelley, and J. Zhang. 2004. How flexibility induces streamlining in a two-
682 dimensional flow. Phys. Fluids **16:** 1694-1713, doi:10.1063/1.1668671

683 Barko, J. W., and W. James. 1998. Effects of submerged aquatic macrophytes on nutrient
684 dynamics, sedimentation, and resuspension, p. 197-214. *In* E. Jeppesen, M. A. Sondergaard, M.
685 O. Sondergaard, and K. Christoffersen [eds.], The structuring role of submerged macrophytes in
686 lakes. Springer Verlag.

687 Boller, M. L., and E. Carrington. 2006. The hydrodynamic effects of shape and size change
688 during reconfiguration of a flexible macroalga. J. Exp. Biol. **209:** 1894-1903,
689 doi:10.1242/jeb.02225

690 Bouma, T. J., M. B. De Vries, E. Low, G. Peralta, C. Tanczos, J. Van de Koppel, and P. M. J.
691 Herman. 2005. Trade-offs related to ecosystem engineering: A case study on stiffness of
692 emerging macrophytes. Ecology. **86:** 2187-2199.

693 Bradley, K., and C. Houser. 2009. Relative velocity of seagrass blades: Implications for wave
694 attenuation in low-energy environments. J. Geophys. Res. -Earth Surf. **114:** F01004,
695 doi:10.1029/2007JF000951

696 Blevins, R. D. 1984. Applied fluid dynamics handbook. Van Nostrand Reinhold.

697 Carpenter, S. R., and D. M. Lodge. 1986. Effects of submersed macrophytes on ecosystem
698 processes. Aquat. Bot. **26:** 341-370.

699 Costanza, R., R. d'Arge, R. de Groot, S. Farber, M. Grasso, B. Hannon, K. Limburg, S. Naeem,
700 R. V. O'Neill, J. Paruelo, R. G. Raskin, P. Sutton, and M. van den Belt. 1997. The value of the
701 world's ecosystem services and natural capital. Nature **387:** 253-260.
702 de Boer, W. F. 2007. Seagrass-sediment interactions, positive feedbacks and critical thresholds
703 for occurrence: A review. Hydrobiologia. **591:** 5-24, doi:10.1007/s10750-007-0780-9
704 de Langre, E. 2008. The effects of wind on plants: A review. Annu. Rev. Fluid Mech. **40:** 141-
705 168, doi:10.1146/annurev.fluid.40.111406.102135
706 Denny, M., B. Gaylord, and E. Cowen. 1997. Flow and flexibility - II. The roles of size and
707 shape in determining wave forces on the bull kelp Nereocystis luetkeana. J. Exp. Biol. **200:**
708 3165-3183.
709 Denny, M., B. Gaylord, B. Helmuth, and T. Daniel. 1998. The menace of momentum: Dynamic
710 forces on flexible organisms. Limnol. Oceanogr. **43:** 955-968.
711 Denny, M., and B. Gaylord. 2002. The mechanics of wave-swept algae. J. Exp. Biol. **205:** 1355-
712 1362.
713 Dijkstra, J. T., and R. E. Uittenbogaard. 2010. Modeling the interaction between flow and highly
714 flexible aquatic vegetation. Water Resour. Res. **46:** W12547, doi:10.1029/2010WR009246
715 Folkard, A. M. 2005. Hydrodynamics of model Posidonia oceanica patches in shallow water.
716 Limnol. Oceanogr. **50:** 1592-1600.
717 Fonseca, M. S., and J. S. Fisher. 1986. A comparison of canopy friction and sediment movement
718 between 4 species of seagrass with reference to their ecology and restoration. Mar. Ecol. -Prog.
719 Ser. **29:** 15-22.
720 Fonseca, M. S., J. S. Fisher, J. C. Zieman and G. W. Thayer. 1982. Influence of the seagrass
721 *Zostera marina* L., on current flow. Estuar. Coast. Shelf Sci. **15:** 351-364.

722 Fonseca, M. S., and W. J. Kenworthy. 1987. Effects of current on photosynthesis and distribution
723 of seagrasses. Aquat. Bot. **27:** 59-78.
724 Fonseca, M. S. 1998. Exploring the basis of pattern expression in seagrass landscapes. Ph.D.
725 thesis. Univ. of California, Berkeley.
726 Fonseca, M. S., M. A. R. Koehl, and B. S. Kopp. 2007. Biomechanical factors contributing to
727 self-organization in seagrass landscapes. J. Exp. Mar. Biol. Ecol. **340:** 227-246,
728 doi:10.1016/j.jembe.2006.09.015
729 Ghisalberti, M., and H. M. Nepf. 2002. Mixing layers and coherent structures in vegetated
730 aquatic flows. J. Geophys. Res. -Oceans **107:** 3011, doi:10.1029/2001JC000871
731 Gosselin, F., E. de Langre, and B. A. Machado-Almeida. 2010. Drag reduction of flexible plates
732 by reconfiguration. J. Fluid Mech. **650:** 319-341, doi:10.1017/S0022112009993673
733 Green, J. C. 2005. Further comment on drag and reconfiguration of macrophytes. Freshwat. Biol.
734 **50:** 2162-2166, doi:10.1111/j.1365-2427.2005.01470.x
735 Harder, D. L., O. Speck, C. L. Hurd, and T. Speck. 2004. Reconfiguration as a prerequisite for
736 survival in highly unstable flow-dominated habitats. J. Plant Growth Regul. **23:** 98-107,
737 doi:10.1007/s00344-004-0043-1
738 Hurd, C. L. 2000. Water motion, marine macroalgal physiology, and production. J. Phycol. **36:**
739 453-472.
740 Koehl, M. A. R. 1984. How do benthic organisms withstand moving water. Am. Zool. **24:** 57-70.
741 Kouwen, N., and T. Unny. 1973. Flexible roughness in open channels. J. Hydraul. Div. **99:** 713-
742 728.
743 Kundu, P. K., and I. M. Cohen. 2005. Fluid mechanics, 3rd ed. Elsevier.

744 Luhar, M., S. Coutu, E. Infantes, S. Fox, and H. Nepf. 2010. Wave-induced velocities inside a
745 model seagrass bed. J. Geophys. Res. -Oceans **115:** C12005, doi:10.1029/2010JC006345
746 Luhar, M., J. Rominger, and H. Nepf. 2008. Interaction between flow, transport and vegetation
747 spatial structure. Environ. Fluid Mech. **8:** 423-439, doi:10.1007/s10652-008-9080-9
748 Madsen, J. D., P. A. Chambers, W. F. James, E. W. Koch, and D. F. Westlake. 2001. The
749 interaction between water movement, sediment dynamics and submersed macrophytes.
750 Hydrobiologia. **444:** 71-84.
751 Mass, T., A. Genin, U. Shavit, M. Grinstein, and D. Tchernov. 2010. Flow enhances
752 photosynthesis in marine benthic autotrophs by increasing the efflux of oxygen from the
753 organism to the water. Proc. Natl. Acad. Sci. U. S. A. **107:** 2527-2531,
754 doi:10.1073/pnas.0912348107
755 Nikora, V. 2010. Hydrodynamics of aquatic ecosystems: an interface between ecology,
756 biomechanics and environmental Fluid Mechanics. River Res. Appl. **26:** 367-384,
757 doi:10.1002/rra.1291
758 Penhale, P. A., and R. G. Wetzel. 1983. Structural and functional adaptations of eelgrass
759 (Zostera-Marina L) to the anaerobic sediment environment. Can. J. Bot. -Rev. Can. Bot. **61:**
760 1421-1428.
761 Peralta, G., F. G. Brun, J. L. Perez-Llorens, and T. J. Bouma. 2006. Direct effects of current
762 velocity on the growth, morphometry and architecture of seagrasses: a case study on Zostera
763 noltii. Mar. Ecol. -Prog. Ser. **327:** 135-142.
764 Peralta, G., L. A. van Duren, E. P. Morris, and T. J. Bouma. 2008. Consequences of shoot
765 density and stiffness for ecosystem engineering by benthic macrophytes in flow dominated areas:
766 A hydrodynamic flume study. Mar. Ecol. -Prog. Ser. **368:** 103-115.

767 Puijalon, S., G. Bornette, and P. Sagnes. 2005. Adaptations to increasing hydraulic stress:
768 morphology, hydrodynamics and fitness of two higher aquatic plant species. J. Exp. Bot. **56:**
769 777-786, doi:10.1093/jxb/eri063
770 Sand-Jensen, K. 2003. Drag and reconfiguration of freshwater macrophytes. Freshwat. Biol. **48:**
771 271-283.
772 Schouveiler, L., C. Eloy, and P. Le Gal. 2005. Flow-induced vibrations of high mass ratio
773 flexible filaments freely hanging in a flow. Phys. Fluids **17:** 047104, doi:10.1063/1.1878292
774 Statzner, B., N. Lamouroux, V. Nikora, and P. Sagnes. 2006. The debate about drag and
775 reconfiguration of freshwater macrophytes: comparing results obtained by three recently
776 discussed approaches. Freshwat. Biol. **51:** 2173-2183, doi:10.1111/j.1365-2427.2006.01636.x
777 Stewart, H. L. 2006. Morphological variation and phenotypic plasticity of buoyancy in the
778 macroalga Turbinaria ornata across a barrier reef. Mar. Biol. **149:** 721-730, doi:10.1007/s00227-
779 005-0186-z
780 Stewart, H. L. 2004. Hydrodynamic consequences of maintaining an upright posture by different
781 magnitudes of stiffness in buoyancy in the tropical alga *Turbinaria ornata*. J. Mar. Syst. **49:** 157-
782 167.
783 Stoer, J., and R. Bulirsch. 2002. Introduction to numerical analysis, 3rd ed. Springer-Verlag.
784 Sukhodolov, A. 2005. Comment on drag and reconfiguration of macrophytes. Freshwat. Biol.
785 **50:** 194-195, doi:10.1111/j.1365-2427.2004.01296.x
786 Vogel, S. 1994. Life in moving fluids. Princeton University Press.
787 Zimmerman, R. C. 2003. A biooptical model of irradiance distribution and photosynthesis in
788 seagrass canopies. Limnol. Oceanogr. **48:** 568-585.

Tables

Table 1. List of test cases for the model blade experiments.

	l (cm)	B	Ca							
			U (cm s^{-1})							
			3.6	7.1	11	14	16	22	27	32
HDPE	5	0.0049	0.032	0.12	0.28	0.50	0.66	1.2	1.8	2.5
E = 0.93±0.08 GPa	10	0.040	0.25	0.99	2.2	4.0	5.3	9.3	15	20
$\Delta\rho$ = 50±10 kg m^{-3}	15	0.13	0.86	3.3	7.5	14	18	32	50	68
b = 1.0±0.05 cm	20	0.32	2.0	7.9	18	32	42	75	120	160
t = 0.4±0.04 mm	25	0.62	3.9	15	35	63	83	150	230	320
Silicon foam	5	2.7	0.55	2.1	4.8	8.7	11	20	32	44
E = 500±60 kPa	10	22	4.4	17	38	70	92	160	260	350
$\Delta\rho$ = 330±50 kg m^{-3}	15	73	15	58	130	240	310	550	860	1200
b = 1.0±0.05 cm	20	170	36	140	310	560	730	1300	2000	2800
t = 1.9±0.10 mm	25	340	69	270	600	1100	1400	2500	4000	5500

Table 2. Assumed seagrass blade properties to generate the model predictions (Fig. 7) for comparison to the data reported in Fonseca and Kenworthy (1987).

Species	b (cm)[1]	t (mm)[1]	l (cm)	E (GPa)[2]	$\Delta\rho$ (kg m^{-3})	B
Thalassia testudinum	1.0	0.45	20[1] (10 – 30)	1.0 (0.4 – 2.4)	85[2]	0.40 (0.02 – 3.3)
Halodule wrightii	0.2	0.40	15[1] (10 – 20)	1.0 (0.4 – 2.4)	85[2]	0.20 (0.03 – 1.3)
Zostera marina	0.8	0.35	40[3] (30 – 50)	1.0 (0.4 – 2.4)	325[3]	20 (3.5 – 98)

Source: [1]Luhar et al. (2010); [2]Bradley and Houser (2009); [3]Abdelrhman (2007)

Table 3. Material and geometric properties for the macroalga *Turbinaria ornata*, as reported by Stewart (2006). Also shown are the estimated buoyancy parameter and range of Cauchy number. A negative value of the buoyancy parameter corresponds to the case where the vegetation is denser than the water.

	Backreef	Forereef
E (MPa)	29	34
l (cm)	19	9.9
r (mm)	1.3	1.6
A (cm^2)*	12	7.0
F_B (mN)	23	-10
B	15	-0.56
Ca (U = 32 – 75 cm s^{-1})	76 – 400	4.0 – 21

* Indirect estimate based on other reported properties

Figure Legends

Figure 1. Schematic showing the coordinate system and force balance used to derive the mathematical model for the flow-induced reconfiguration of aquatic vegetation.

Figure 2. Model predictions for the effective blade length (l_e/l) and blade posture. (a) Effective blade length plotted against the ratio of hydrodynamic forcing and blade buoyancy ($B^{-1}Ca$), for zero-stiffness blades. Also shown are predicted blade postures for the cases marked with a dot: $B^{-1}Ca = 0.1$ and $B^{-1}Ca = 3.2$. (b) Effective blade length plotted against the Cauchy number (Ca), for blades that are neutrally buoyant. The blade postures shown in the left and right subplots correspond to the cases marked with a dot, $Ca = 1$ and $Ca = 32$, respectively. (c) Effective blade length plotted against the Cauchy number for four different values of the buoyancy parameter: $B = 0$ (bold black line), 10 (fine black line), 50 (bold gray line), and 100 (fine gray line). The predicted blade postures shown in the subplots correspond to the cases marked with a dot, $Ca = 1$, $Ca = 32$, and $Ca = 1000$, from left to right, respectively.

Figure 3. Schematic of the experimental set-up. Also shown are the measured profiles of velocity for the eight different flow speeds tested in this study (Table 1). Note the vertical exaggeration.

Figure 4. (a) Horizontal force (F_x), plotted against velocity (U), for the model blades made from high density polyethylene (HDPE). The black squares and black line correspond to the measured and predicted forces for the 5 cm-long blade. The gray circles and gray line correspond to the measured and predicted forces for the 25 cm-long blade. (b) Same as (a), but for the model

blades made from silicone foam. (c-f) Observed blade postures for two different flow speeds. The overlaid white curves are model predictions, and the scale bar is 5 cm. (c, e) correspond to the 5 cm- and 25 cm-long HDPE blades, respectively. (d, f) correspond to the 5 cm- and 25 cm-long foam blades.

Figure 5. (a) Effective blade length (l_e/l), plotted as a function of the Cauchy number (Ca), for the model blades made from HDPE. The markers show experimental observations for the five different blade lengths tested, l = 5 cm (squares), 10 cm (asterisks), 15 cm (triangles), 20 cm (crosses), and 25 cm (circles), and the solid lines represent model predictions. The inset legend shows the value for the buoyancy parameter (B) for each of the five blade lengths. (b) Same as (a), but for the model blades made from foam.

Figure 6. (a) Comparison of model predictions for blade posture with the observations made by Abdelrhman (2007) for the seagrass *Zostera marina* exposed to a flow of speed $U = 6$ cm s^{-1}. Predicted blade postures are shown as black curves on the left, while the observations are shown on the right (images from fig. 8 in Abdelrhman 2007). Note that the two predicted blade postures correspond to the highest and lowest assumed values for the blade elastic modulus, as described in the text. (b, c) Same as (a) but for flow speeds $U = 12$ cm s^{-1} and $U = 14$ cm s^{-1}, respectively.

Figure 7. (a-c) Deflected blade height (h/l), plotted against velocity (U). Observations made by Fonseca and Kenworthy (1987) are shown as squares, while the model predictions are shown as solid and dashed lines. The solid line corresponds to model predictions that use the elastic modulus and blade length that are in the middle of the range reported in previous literature. The

dashed lines correspond to predictions made with the upper- and lower-limit of elastic modulus and blade length (Table 2). (a) shows the data for the seagrass species *Thalassia testudinum*, while (b, c) show the data for *Halodule wrightii* and *Zostera marina*, respectively.

Figure 8. Effective blade length (l_e/l) plotted against velocity (U) for the marine macroalga *Turbinaria ornata*. The black squares correspond to the measurements made by Stewart (2006) for samples collected from a wave-exposed, forereef site, while the gray circles correspond to the measurements for samples collected from a sheltered, backreef site. The black and gray lines show model predictions for the forereef and backreef samples, respectively. The shaded areas represent the velocities reported by Stewart (2006) for each site.

Figure 9. Reconfiguration response for three different velocity profiles. (a) Schematic of the three velocity profiles: the depth-uniform case (solid line), the dense canopy case (bold dashed line), and the sparse canopy case (fine dashed line). (b) Deflected canopy height (h/l) plotted against the Cauchy number (Ca) for two values of the buoyancy parameter, $B = 0$ (black lines) and $B = 100$ (gray lines). The solid lines denote the depth-uniform case while the bold and fine dashed lines correspond to the dense and sparse canopy cases. (c) Similar to (b) but showing the effective length (l_e/l) plotted against the Cauchy number (Ca).

Figure 10. Effective blade length (l_e/l) plotted against the Cauchy number (Ca) for a range of values of the buoyancy parameter, $B = 0$ (bold black line), 10 (fine black line), 50 (bold gray line), and 100 (fine gray line). The solid lines denote predictions made by the numerical model, while the dashed lines correspond to the empirical relationship shown in Eq. 16.

Figure 1

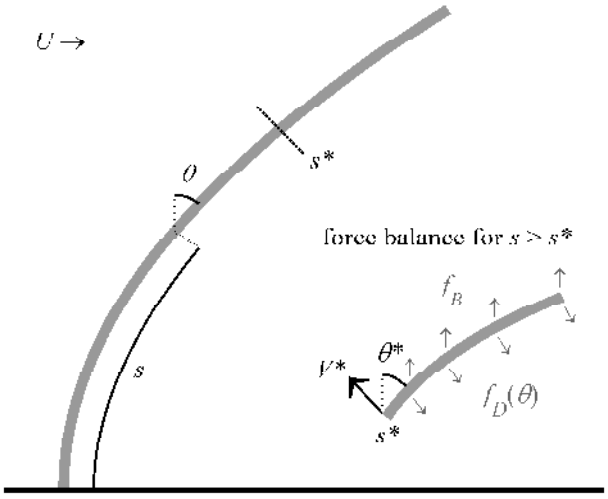

Figure 2

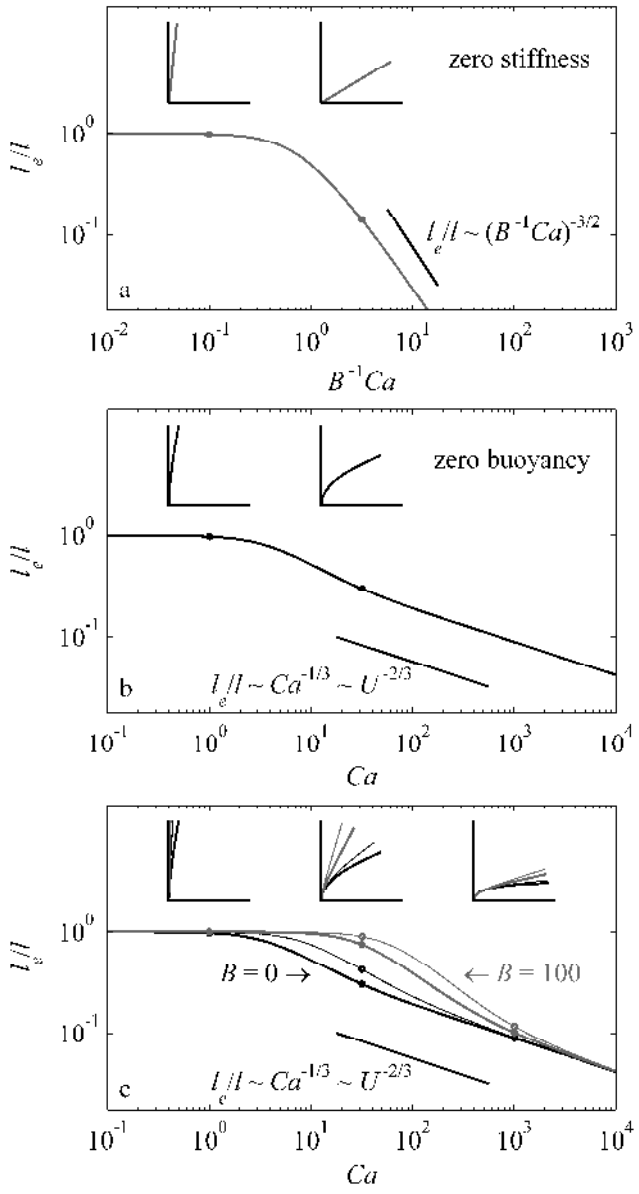
zero stiffness
l_e/l
10^0
10^{-1}
$l_e/l \sim (B^{-1}Ca)^{-3/2}$
a
10^{-2} 10^{-1} 10^0 10^1 10^2 10^3
$B^{-1}Ca$
zero buoyancy
l_e/l
10^0
10^{-1}
b
$l_e/l \sim Ca^{-1/3} \sim U^{-2/3}$
10^{-1} 10^0 10^1 10^2 10^3 10^4
Ca
l_e/l
10^0
10^{-1}
$B = 0 \rightarrow$
$\leftarrow B = 100$
c
$l_e/l \sim Ca^{-1/3} \sim U^{-2/3}$
10^{-1} 10^0 10^1 10^2 10^3 10^4
Ca

Figure 3

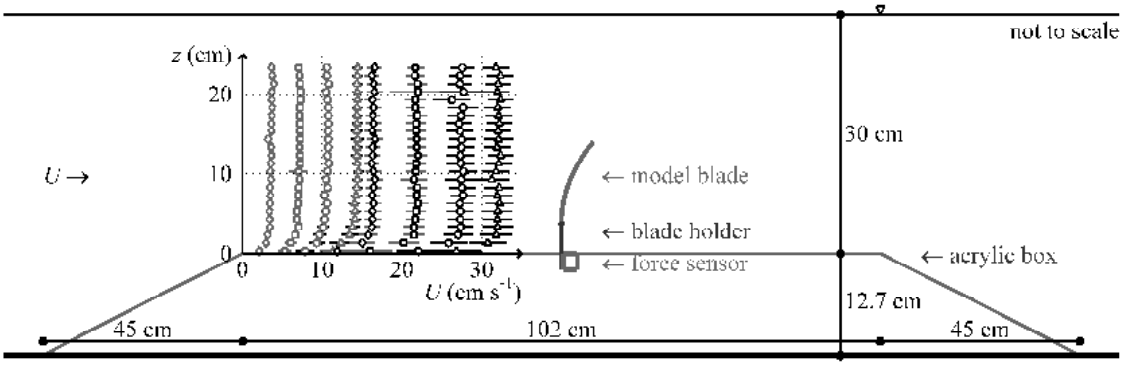
not to scale
z (cm)
20
10
0
0
10
20
30
U (cm s-1)
U →
30 cm
← model blade
← blade holder
← force sensor
← acrylic box
12.7 cm
45 cm
102 cm
45 cm

Figure 4

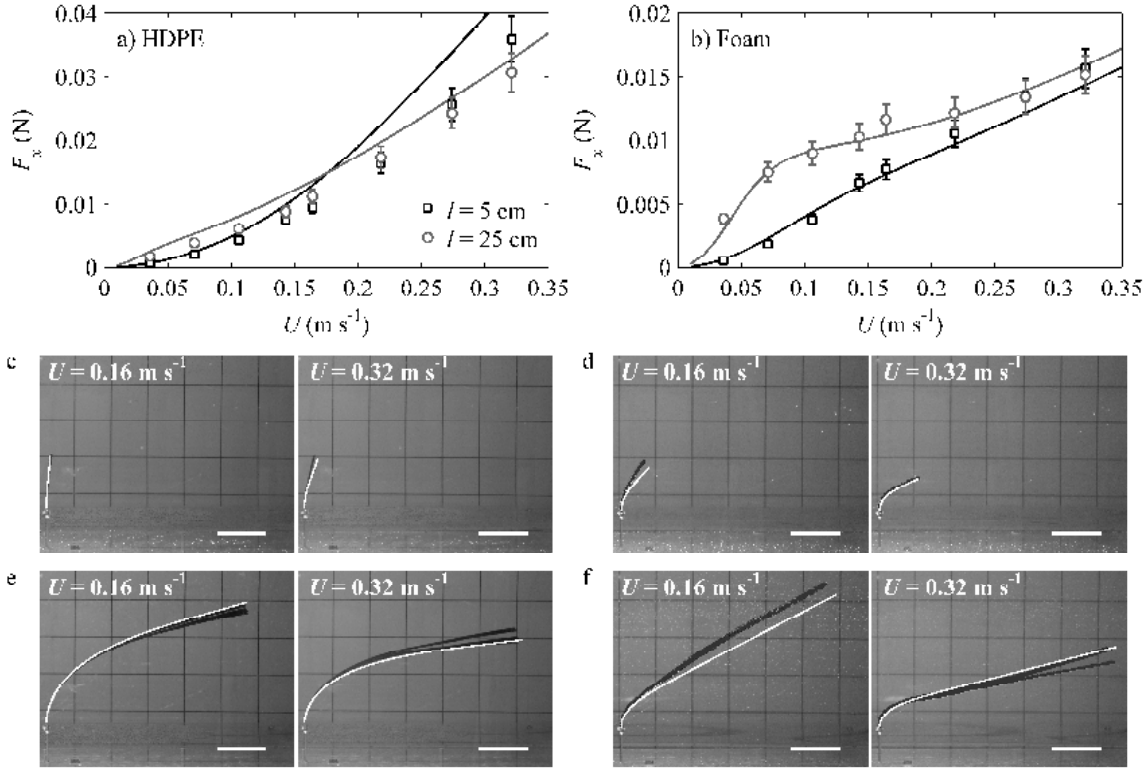

Figure 5

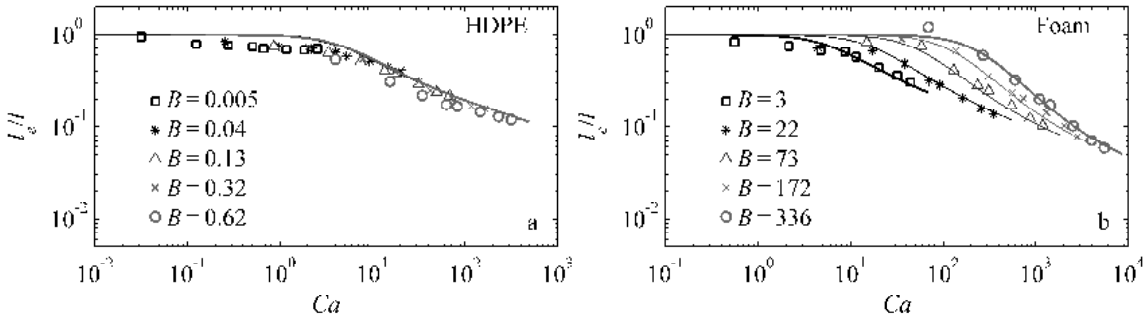
HDPE
B = 0.005
B = 0.04
B = 0.13
B = 0.32
B = 0.62
a
Foam
B = 3
B = 22
B = 73
B = 172
B = 336
b
Ca
Ca

Figure 6

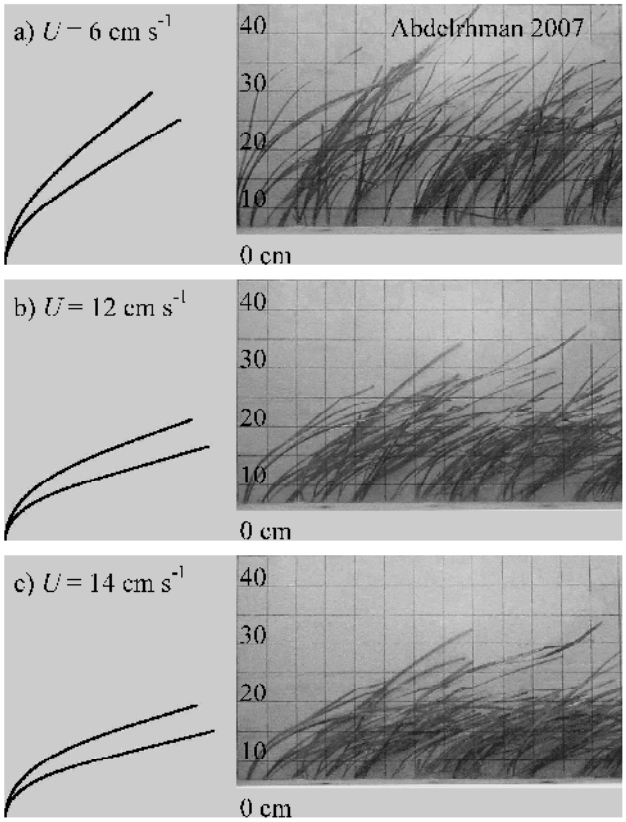
a) $U = 6$ cm s^{-1}
40
30
20
10
Abdelrhman 2007
0 cm
b) $U = 12$ cm s^{-1}
40
30
20
10
0 cm
c) $U = 14$ cm s^{-1}
40
30
20
10
0 cm

Figure 7

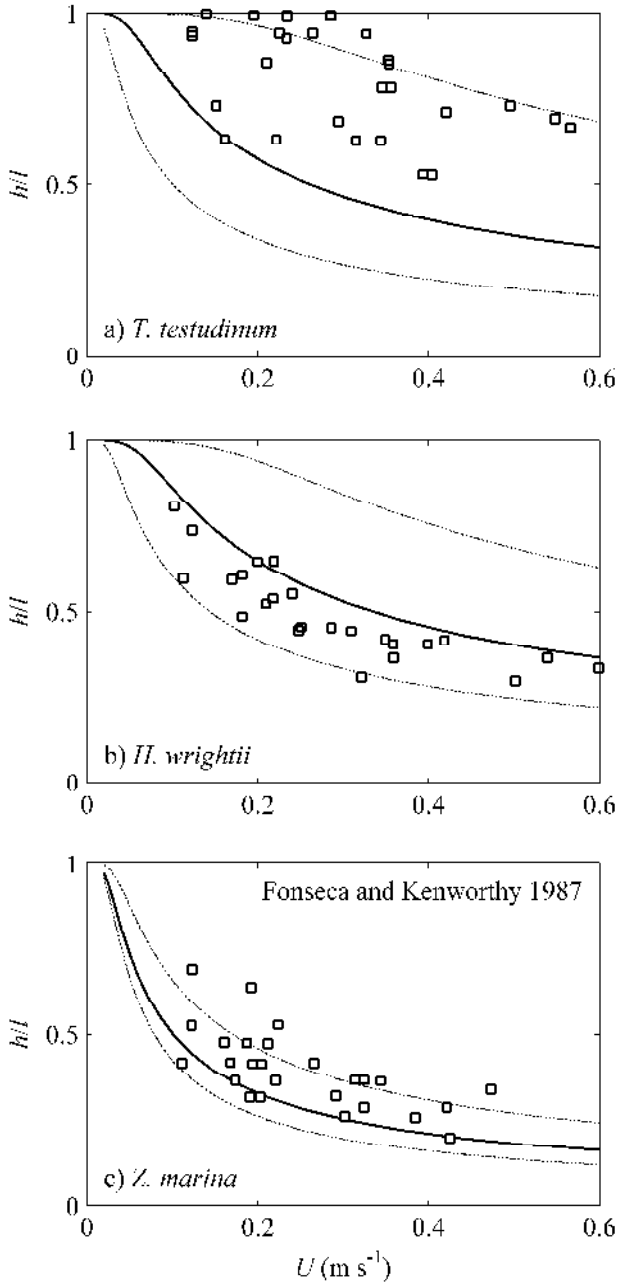
h/l
1
0.5
0
0
0.2
0.4
0.6
a) T. testudinum
b) H. wrightii
Fonseca and Kenworthy 1987
c) Z. marina
U (m s-1)

Figure 8

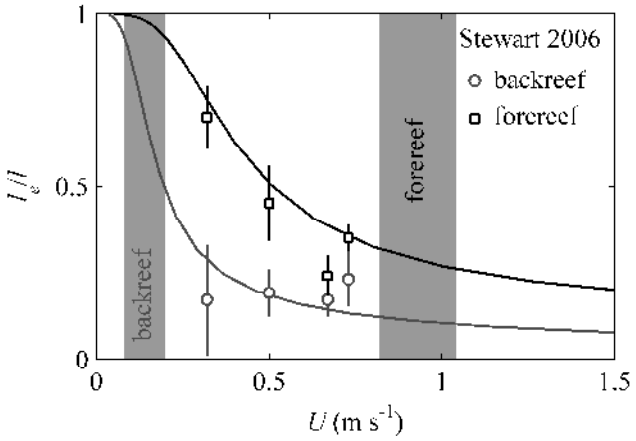
Stewart 2006
backreef
forereef
backreef
forereef
I/I_e
U (m s^{-1})
0
0.5
1
1.5

Figure 9

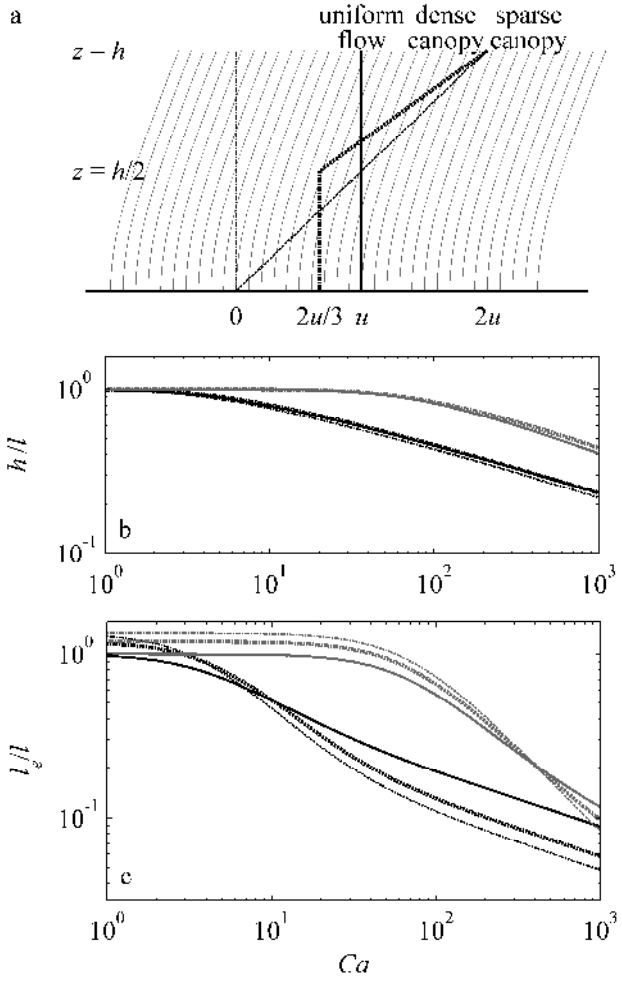
a
uniform flow
dense canopy
sparse canopy
z – h
z = h/2
0
2u/3
u
2u
h/l
10^0
10^-1
b
10^0
10^1
10^2
10^3
l_e/l
10^0
10^-1
c
10^0
10^1
10^2
10^3
Ca

Figure 10